The response of reworked aerosols to climate through estimation of inter-particle forces

Assadi Langroudi, Arya; Jefferson, Ian

DOI:
10.1007/s13762-016-0958-7

Document Version
Peer reviewed version

Citation for published version (Harvard):
Assadi Langroudi, A & Jefferson, I 2016, 'The response of reworked aerosols to climate through estimation of inter-particle forces', *International Journal of Environmental Science and Technology*.
https://doi.org/10.1007/s13762-016-0958-7

Title. The response of reworked aerosols to climate through estimation of inter-particle forces

Short title. Significance of moisture in dust flux trigger

Arya ASSADI LANGROUDI [corresponding author]

Lecturer – The School of Architecture, Computing and Engineering, the University of East London, Docklands, London, England

Email address: A.AssadiLangroudi@uel.ac.uk

Ian JEFFERSON

Professor – College of Engineering and Physical Sciences, the University of Birmingham, Birmingham, England

Email address: i.jefferson@bham.ac.uk

Tel. +44 (0) 121 414 7972

Abstract.

This paper describes the first use of inter-particle force measurement in reworked aerosols to better understand the mechanics of dust deflation and its consequent ecological ramifications. Dust is likely to carry hydrocarbons and micro-organisms including human pathogens and cultured microbes, thereby is a threat to plants, animals and human. Present day global aerosol emissions are substantially greater than in 1850, however the projected influx rates are highly disputable. This uncertainty, in part, has roots in the lack of understanding of deflation mechanisms. A growing body of literature shows that whether carbon emission continue to increase, plant-transpiration drops and soil water retention enhances, allowing more greenery to grow and less dust to flux. On the other hand, a small but important body of geochemistry literature shows that increasing emission and global temperature leads to extreme climates, decalcification of surface soils containing soluble carbonate polymorphs and hence a greater chance of deflation. The consistency of loosely-packed reworked silt loose provides background data against which the resistance of dust's bonding components (carbonates and water) can be compared. The use of macro-scale phenomenological approaches to measure dust consistency is trivial. Instead, consistency can be measured in terms of inter-particle stress state. This paper describes a semi-empirical parametrisation of the inter-particle cohesion forces in terms of the balance of contact-level forces at the instant of particle motion. We put forward the hypothesis that the loss of Ca^{2+}-based pedogenic salts is responsible for much of the dust influx and surficial drying pays a less significant role.

Key words: dust, deflation, menisci, pedogenic, inter-particle forces

1. Introduction

The World Health Organization estimated an annual 1.3 million deaths as a result of air pollution, the most significant type of which is particulate matter (USEPA 2013) with an estimated mean annual global flux of 1020 to 2070 Tg (Miller et al. 2004; Ginoux et al. 2004) and 1 to 3.6 Pg yr^{-1} mobilization rate (Maher et al. 2010), out of which 1500 Tg settles on land when physio-chemical processes favour the down flux (Shao et al. 2011). The resistance of dust to deflation (i.e. saltation) has been numerically modelled in several works (Smalley 1970; Marticorena et al. 1997; Alfaro et al. 1998; Creyssels et al. 2009; etc) and experimentally measured - at macro-scale - in terms of flux-crust strength (Goossens D. 2004). Yet, the mechanics of accumulated dust transformation from unstable to metastable state is yet poorly known (Svirčev et al. 2013), in part due to the hardship in measurement of *fluid threshold*. The threshold is a function of both gravitational and inter-particle cohesion forces that oppose the particle lifting (Bagnold 1941). A semi-empirical method has been adopted here to explore the relative significance of water menisci and chemical cementation – as two components of the *fluid threshold* - through evoking the well-established physical principles and approximating the Newtonian forces at particle-level.

Dust initially emits from continental areas over periods of semi-aridity and settle when wind intensity decreases over moist and rough lands. Deposited dust then combines with electrically-charged minerals (including clay and ions) to develop metastable open structures, lent by a suite of Newtonian forces including skeletal, weight, hydrostatic, hydrodynamic, and buoyant. Newtonian forces balance capillary and cementation forces (Santamarina, 2003). For a wind erosive force greater than the sum of capillary-cementation forces combined (*fluid threshold*), destabilisation in dust's structure initiates which potentially leads to

deflation. For the relative significance of *fluid threshold* components to be quantified, inter-particle forces need to be measured.

The research into explicit links between macro-scale actions (e.g. water content, net stress) and microscopic features (e.g. contact forces) has been the subject of numerous works, perhaps beginning with the work of Dantu (1957) on mechanisms of load transfer in granular material using optically sensitive discs. Inter-particle forces were expressed by some workers in terms of average stress tensor (Cundall and Strack 1983; Thornton and Barnes 1986), although might be argued as force transmission in granular packings is known to be peculiar and above all, very inhomogeneous. The latter shortfall was filled later in a number of models including the Claudin et al. (1998). Much of the parametrisation equations for inter-particle force has been reported in the aeolian saltation theory literature in an attempt to determine threshold stress for particles lifting into atmosphere. For example, Cornelis et al (2004) formulated (Equation 1) the inter-particle force (F_{ip}) as sum of London dispersion force (K_{vdw} proportionality coefficient times diameter), 'wet' bonding force (a function of surface tension σ, diameter d, and matric suction ψ_m), and effective gravitational force (a function of effective density $\rho_s - \rho_f$, and gravitational moisture content ω). Our recent findings (Assadi and Jefferson 2013) lends some degrees of uncertainty to the latter formulation since first, the model does not consider the implications of packing's change – and double porosity – and secondly, the model is based on three-phase solid-air-liquid systems and excludes chemical cementation forces as a component of cohesive inter-particle force. In the more recent Ravi et al (2006) study, emphasis was kept on soil water retention (Equation 2) in clean granular systems considering the water retention properties. They accommodated a

van den Waals force $\beta_c d$ component together with the capillary force in their equation but did not take the implications of chemical cementation forces into account.

$$F_{ip} = K_{vdw}.d + \frac{K_{AC}.\sigma^2.d^2}{|\psi_m|} + (1+\omega)K_G(\rho_s - \rho_f)gd^3 \quad (1)$$

$$F_{ip} = d\left[\pi\left(\frac{c}{\rho_w\sigma}\left(\frac{RT}{M}\right)^{-b}\left(ln\frac{RH}{100}\right)^{-b} - \frac{y}{2}\right)\right]\frac{RT}{M} \times ln\left(\frac{RH}{100}\right) + \beta_c d \quad (2)$$

Ishizuka et al (2008) further extended the formulations and introduced σ_m, which is a function of the soil plastic pressure, hardness of ground, or crust binding force. They then reported a direct relationship between hardness function, $\rho_b\Omega/m = \sigma_m$ (normalized against mass of impacting particles), and rate of dust emission (Equation 3).

$$\tilde{F}(D_i, D_s) = c_y\left[(1-\gamma) + \gamma\frac{\rho_m(D_i)}{\rho_f(D_i)}\right]\frac{\hat{Q}g}{u_*^2 m}\left(\rho_b\eta_{fi}\Omega + \eta_{ci}m\right) \quad (3)$$

One important milestone in mechanics of granular materials at grain scale was the inception of discrete element method (DEM) introduced by Cundall and Strack (1979), which was followed by a thread of statistical approaches to measure inter-particle forces (Guo and Zhao 2013; Ostojic et al. 2006). Discrete models however lack in their reliance on computational power, forcing workers to resort to enlarging the particles and calibrating the model, and in the use of spheres and ellipsoids, which leads to negligence of the grain angularity (Andrade and Tu 2009). The restriction of direct measurement technologies in measuring contact forces within colloidal suspensions, motivates the use simple principles of physics to capture the particle-level phenomena.

This paper describes a semi-empirical parametrisation of the inter-particle cohesion forces in a loosely cemented Aeolian silt in terms of the balance of contact-level forces at the instant

of particle motion. Much of the links between the macro- and micro-parameters are developed and presented for a homogeneous two-dimensional analogy of assemblies of spheres, an extension of the well-known Santamarina (2003) equation.

The simplicity of the method offers the chance to reader to replicate the experiments. Despite assuming particles as mono-dispersed spheres, which is a strong assumption, the process is able to represent the macroscopic behaviour of aerosol materials under relatively well controlled and homogeneous conditions, not untypical to much of the PM_{10-20} aeolian deposits.

2. Materials and Methods

2.1 Testing materials

Silt-sized quartz particulate matter (PM) was artificially produced through grinding dry clean (washed with Calgon: 33g Sodium Hexametaphosphate and 7g Sodium Carbonate in 1 litre distilled water) 1.15mm (peak on 0.5-0.6mm) in diameter Leighton Buzzard Lower Greensand in a Sientechnik 800W TS1000 disc mill (Assadi et al. 2014) followed by gravity sedimentation using Stoke's law to omit the sub-2µm and >63µm tails as explained in Lamb (1994) and initially practiced in similar fashion by Assallay (1998). Grinding input (energy-duration) was tailored, via try and error, to generate a peak on 10-20µm size of the ground sand. Mode size distribution was captured using a Sympatec laser diffraction machine using a 1.544 refractive index at a 99.73% degree of confidence (O'Hara-Dhand et al. 2013). Ground sand was crumbled and mixed dry with kaolinite (PolWhite-E containing 74-80% kaolin, 2-3% Montmorillonite, 5-12% Feldspar, 5-15% Mica, and 1-2% Quartz) and Anhydrous Sodium Carbonate at Silt:70|Clay:10|Carbonate:20 per cent by weight proportion to produce a benchmark sub-63µm dry saline dust material. Under controlled ambient conditions (relative

humidity and temperature), dust was pluviated into a 75mm oedometer ring at a constant rate and freefall height. Distilled water was finely sprayed on the surface of freshly deposited dust (for every 2mm high dust column). Trimmed Aeolian specimen was axially loaded to a 12.5kPa seating pressure before a 48 hours drying course at 75-85°C temperature. To replicate the reworking process, a dilute 0.4M (110.98 g/mol modal mass) Calcium Chloride solution (pH=8.0) was introduced to the dry specimen from the lower drain point for 8 hours before a subsequent drying at 75-85°C. Chemical curing was repeated two more times to generate a combination of Aragonite and Calcite carbonates within the dust structure (verified through X-ray diffraction and energy-dispersive X-ray spectroscopy in Assadi (2014)). The reworked dust product was eventually dried to 0.4% hygroscopic water content and a void ratio of 1.19-1.41 (unit weight of 11.0 to 12.1kN/m^3), not untypical of much of the globally distributed deposited silt-sized aerosols. Mode size distribution of testing material is illustrated in Figure 1.

Fig. 1

2.2 Testing procedures

Thirteen free oedometer tests (ASTM 2014; BS 1990) were performed on identical specimens, through wetting (from the lower drain point by the act of capillary) for 0.75, 1.5, 2, 2.25, 3, 5, 7, 10, 80, 160, 320, 720, and 1527 minutes. Water content was recorded at the end of each experiment. The fourteenth specimen was assembled in the oedometer cell, equipped with a graduated pipette that passed vertically through the flanged top disc to the bottom of the chamber. In an attempt to examine the implications of groundwater flow at grain-scale, a steady state flow (70-minutes) followed by hydrostatic condition was simulated under a net stress slightly lower than the swelling pressure. The specimen's height (and

hence void ratio) was recorded against the wetting time upwards from 0 second at intervals of ten seconds.

2.3 Model development

2.3.1 Skeletal force

A simple soil fabric model (i.e. domain) was adopted to approximate the skeletal force at grain-level from net stress. d-sized cubic clusters were aligned in chains along three Cartesian axes. Each column of clusters was surrounded by a neighbouring column of 'void' d-sized cubes, representing the macro-pores (Fig 2). To build a suite of solid-void combinations, void cubes were allowed to accommodate sub d-size solid cubes. Also, solid cubes were allowed to accommodate sub d-size void cubes. Sub d-size void cubes represent micro-pores. The effective area (A_e) was defined as solid occupancy in every 2d-sized square area. The effective area was considered as the region of solids that carry the effective stress. Over 50 solid-void combination cases were collated into an inventory of void ratio versus effective area. The 'cubic expression' was converted into a 'spherical expression' by presuming equal surface areas in vertical projection (Equation 4).

$$d_{squ.}{}^2 = \frac{1}{2} 4\pi \left(\frac{d_{sph.}}{2}\right)^2 : d_{squ.} \approx d_{sph.}\sqrt{\frac{\pi}{2}} \tag{4}$$

where d_{squ} is width of a cube surrounding a sphere particle of d_{sph} in diameter. In two-dimension, skeletal force at grain-scale was expressed as,

$$\mathrm{F_{(N)skel}} = \sigma'.f\{e,d\} \tag{5}$$

where $f\{e,d\}$ is a function of void ratio (e) and particle mean diameter (d). The built e-A_e inventory (partly reported in Table 1) was inputted into a non-linear regression calculation

using the Levenberg-Marquardt algorithm, to express the $f\{e,d\}$ in the exponential form of Equation 6.

$$f\{e,d\} = \frac{\pi}{2} d^2 . A . exp\left(B . e + C\sqrt{e}\right) \quad (6)$$

where A, B, and C are fitting parameters. Figure 2 shows an example of the defined simple soil fabric model.

Fig. 2

Table 1

2.3.2 Buoyant, weight and hydro-static force

For wetting times less than the time needed for the waterfront to travel the soil column to mid-height, the dry state of grains was imitated with zero buoyant, hydro-static and hydro-dynamic force. Within the framework of physical principles accepted to date,

$$B = \frac{1}{6} \times \pi \times \gamma_w \times D_{50}^3 \qquad for\ t > {}^{t_1}/_2 \quad (7)$$

$$U = 0.5 \left(\frac{\dot{H}_i}{2} + \dot{H}\right) . \rho_w . 4\pi . \left(\frac{D_{50}}{2}\right)^2 \qquad for\ t \geq t_1 \quad (8)$$

$$W = \sum W_j = \frac{\dot{H}_i}{2D_{50}} \times \frac{1}{6} \times \pi \times \gamma_w \times G_s \times D_{50}^3 \quad (9)$$

where 'B' is the buoyant force, t_1 is the time elapsed between the arrival of the water at the top of the specimen and the beginning of the percolation at the lower drain point, 'U' is the hydrostatic force, $\dot{H}_i$ is the specimen height (varied), $\dot{H}$ is water overhead, and 'W' is the weight force. The weight force was assumed compressive and aligned with the gravity

direction. The buoyant force was assumed tensile, reducing either the skeletal or weight forces. Volumetric contraction was mirrored in declining timed trend of hydrostatic force.

2.3.3 Hydro-dynamic force

The Stoke's law at low Reynolds numbers (Bear 1972; Graf 1984; Santamarina 2003), was here utilised to express the hydro-dynamic force as in Equation 10.

$$D = 3\pi \times \mu \times V \times d = 3\pi \times 10^{-3} \times D_{50} \times \frac{K_i \times i_i}{n_i} \tag{10}$$

where $\mathrm{K_i}$ is the full function hydraulic conductivity at wetting time $\mathrm{t = t_i}$, $\mathrm{n_i}$ is the porosity, $\mathrm{D_{50}}$ is the mean particle size and $\mathrm{i_i}$ is the hydraulic gradient as expanded in Equation 11 for three scenarios (1) $\mathrm{0 \le t < {t_1}/_2}$ immediately after wetting, (2) $\mathrm{{t_1}/_2 \le t < t_1}$ steady state flow, and (3) $\mathrm{t \ge t_1}$ constant head state.

$$\forall\ 0 \le t < {t_1}/_2 \Rightarrow\ i = 0 \tag{11}$$

$$\forall\ t = {t_1}/_2\ \Rightarrow\ i = \frac{\Delta H}{H} = \frac{H_w - (t_{SL} + \frac{\dot{H}_\iota}{2})}{\dot{H}_\iota/_2}$$

$$\forall\ {t_1}/_2 < t < t_1 \Rightarrow\ \ i = \frac{\Delta H}{H} = \frac{H_w - (t_{SL} + {3}/_4 H'_i)}{{3}/_4 H'_i}$$

$$\forall\ t = t_1 \Rightarrow\ \ i = \frac{\Delta H}{H} = \frac{H_w - (t_{SL} + H''_i)}{H''_i}$$

$$\forall\ t > t_1\ \Rightarrow i = \frac{\Delta H}{H} = \frac{H_w - \left(t_{SL} + \dot{\mathrm{H}}_\mathrm{i}\right)}{\dot{\mathrm{H}}_\mathrm{i}}$$

where t_{SL} is the height of the oedometer lower porous disc, H''_i is the height of the specimen at $t = t_1$, H'_i is the height of the specimen at $t = {3t_1}/{4}$, and H_w is the height of the water column in the oedometer chamber.

The full function hydraulic conductivity was estimated using Darcy law for the measured degree of saturation, void ratio and hydraulic gradient, assuming a linear relationship between wetting front advancement and wetting time.

2.3.4 Capillary force

Depending on the degree of saturation, unsaturated soils follow either pendular or funicular regimes corresponding to low or high level of water contents, respectively. At both states, liquid bridges form between particles. Liquid bridge units impact the soil structure through developing tensile forces at particle level. The geometry of the liquid bridge is often described by the Laplace-Young equation. In this context, tensile forces depend on inter-particle separation distance, liquid bridge curvature and particle radii. A history of early to recent studies on liquid bridges is brought in Harireche et al. (2013). Here, the funicular state capillary force (F_{cap}) was estimated using the Laplace's differential equation for unique curvature radii (Santamarina 2003) as shown in Equation 12.

$$F_{cap} = \frac{T_s}{d_{pore}} \times 0.5 \times \left[4\pi \left(\frac{D_{50}}{2}\right)^2\right] = \frac{\pi \times D_{50}^2 \times T_s}{2d_{pore}} \quad (12)$$

where d_{pore} denotes the mean pore size (i.e. corresponding with the D_{50}) and T_s is the surface tension for water-air interface in ambient conditions (Fredlund and Rahardjo 1993). The mean pore diameter here was calculated using the Arya-Paris pedo-transfer function (Arya et al. 1999; Arya and Paris 1981; Arya and Paris 1982; Haverkamp and Parlange 1982).

The function involves dividing the cumulative particle-size distribution curve into a number of fractions, each representing a mean pore radius ($\mathrm{r_i}$) and water pressure head (ψ_i). Arya and Paris (1981) proposed a nonlinear expression to relate the pore radius (r_i) to the mean particle radius (R_i):

$$r_i = R_i.\left(\frac{4.e.{n_i}^{1-\alpha}}{6}\right)^{0.5} \tag{13}$$

where e is the void ratio; and n_i is the number of particles in each size fraction derived from:

$$n_i = \frac{W_i}{\left(\frac{4}{3}\pi.{R_i}^3\right).\frac{W_s}{V_s}} = \frac{3W_i}{4\pi.{R_i}^3.\gamma_s} \tag{14}$$

where W_i is the solid mass (per unit sample mass) associated with R_i (i.e. in each given size fraction), in a way that the sum of the W_i is unity. γ_s is the particle density taken equal to $G_s.\gamma_w$, and α_i is the 'scaling factor' (i.e. tortuosity factor). Within the adopted framework, the radius of a given pore is a factor of the mean radius of particles surrounding that pore, in a soil of certain void ratio and specific gravity. For a domain made up of a mesh of equally dimensioned squares, both particles (solids) and pores (voids) can be modelled as squares, the number of which are assumed equal. Hence, the population of the particles can be deemed equal to the population of pores. A sample of calculations are reported in Appendix 1 for interested readers (i.e. supporting document).

The Mikami et al. (1998) pendular state capillary force formulation for smooth sphere pairs is herein practiced, with moderation. Formulation has been inferred from numerical solutions of Laplace-Young Equation together with geometric considerations. The same relation has then been extended to poly-dispersed spheres by Soulié et al. (2006), and expanded herein through integrating the liquid bridge volume for mean pore size in Equations 19-20 (Fig. 3).

$$F_{cap} = \pi \times T_s \times \sqrt{R_1 \times R_2}.\left[c + exp\left(a\frac{D}{R_2} + b\right)\right]$$

$$= \pi.T_s.\sqrt{\left(\frac{D_{50}}{2}\right)^2}.\left[c + exp\left(a \times d_{pore} \times \frac{2}{D_{50}} + b\right)\right] \quad (15)$$

where

$$a = -1.1 \times \left(\frac{V}{R_2^3}\right)^{-0.53} = -1.1 \times \left(V \div \left(\frac{D_{50}}{2}\right)^3\right)^{-0.53} \quad (16)$$

$$b = \left(-0.148Ln\left(\frac{V}{R_2^3}\right) - 0.96\right)\Theta^2 - 0.0082\mathrm{Ln}\left(\frac{V}{R_2^3}\right) + 0.48$$

$$= \left(-0.148Ln\left(V \div \frac{D_{50}{}^3}{2}\right) - 0.96\right) \times \Theta^2 - 0.0082\mathrm{Ln}\left(V \div \frac{D_{50}{}^3}{2}\right) + 0.48$$

$$c = 0.0018Ln\left(\frac{V}{R_2^3}\right) + 0.078 = 0.0018Ln\left(V \div \frac{D_{50}{}^3}{2}\right) + 0.078 \quad (17)$$

$$V = 2R\left(\int_{x_{c1}}^{x_{c2}} y^2\,(x)dx - 2s\right)$$

$$= 2R$$

$$\times \left\{\left[2\int_{-\left(R+\frac{D}{2}-\frac{(r_1+r_2)Rcos\delta}{R+\frac{D}{2}}\right)}^{\left(R+\frac{D}{2}-\frac{(r_1+r_2)Rcos\delta}{R+\frac{D}{2}}\right)}\int_0^{R.sin\delta}(x^2 + y^2 + A^2 - 2Ay - {r_1}^2)^2 dydx\right]\right.$$

$$\left. - 2s\right\} \quad (18)$$

where:

$$s = \frac{\pi.R^2}{360} \times 2\delta - \frac{R^2}{2}.Sin2\delta \quad (19)$$

$$A = (R + r_1).Sin\delta \quad (20)$$

$$\delta = ArcCos\left(\frac{R+\frac{D}{2}}{R+r_1}\right) \quad (21)$$

where Θ is the contact angle between the contractile skin (i.e. zero for pure water and glass after Fredlund and Rahardjo (1993) and between clean quartz grains), r_2 is the internal radius of the principal curvature and r_1 is the external radius, which was estimated from the Laplace equation (Equation 22).

$$(U_a - U_w)_p = T_s \times \left(\frac{1}{r_1} - \frac{1}{r_2}\right) \quad (22)$$

Fig. 3

2.4 Model validity

For this study, particles are assumed mono-dispersed ($d=d_{50}$), spherical in shape, incompressible and non-crushable. The poorly graded PMs with the pronounced mode on 10-20µm lends a good degree of credibility to the incompressibility and integrity of quartz constituents in absence of an external high energy load (Assadi et al. 2014). Forces operate on grain-grain contact points and flow through columns of grains that are aligned into load-carrying paths (Figure 2). Forces were approximated at the mid-height of the testing soil column. Despite appreciating the fact that water front moves within the pore network through preferred water paths (Assadi and Yasrobi 2012); given the closely controlled deposition conditions an even distribution of water was speculated. Because tangential forces contribute to skeletal stresses only to a limited extent (Cundall and Strack 1979), their impact together with the impact of contact moments were neglected in calculations. Concurring with Fratta and Santamarina's (2005) general argument on minimal damping of

force in angular grain assemblies, the sub-angular texture of PMs used justified our assumption of zero damping of force across the specimen.

3. Results and Discussion

The free oedometer experiments as detailed in Section 2.2 allowed the approximation of inter-particle forces for a range of degrees of saturation (associated with matric suction via a wetting-protocol filter paper test). The procedure might be argued to be practical due to the complexity in acquiring identical undisturbed soil specimens, although this drawback can be relaxed by geo-physical profiling (Noborio 2001).

A suite of graphs are presented in this section including the measured wetting timed-trend of void ratio and inter-particle forces for the testing calcareous reworked dust specimen (Figure 4). In the first place, the graphs inform the reader in understanding the structural collapse at the grain scale i.e. the destruction of reworked metastable structure upon wetting, which stands for the threshold of deflation when wind force exceed capillary-cementation bond forces combined. Also, the graphs inform the reader of the reliance of collapse to the total destabilizing Newtonian inter-particle force. Key question in this context is: What is the major cause of reworked dust structural destabilisation at elevated levels of inter-particle forces: A drop in the tensile capillary force or the modification of chemical cementation?

Fig.4

Capillary force initially increased with the advancement of waterfront (Figure 5) while destabilising inter-particle force ($\mathrm{F}_{(\mathrm{N})\mathrm{skel}} - D + W + U - B$) also increased to its peak and dropped thereafter (Figure 6). Structural collapse was captured at a 42% degree of saturation

when the total destabilising inter-particle force (deviatory stress at grain-level) exceeded the capillary and cementation forces combined and sheared the cemented structure. During the wetting process, collapse was captured before capillary and destabilising forces reached their maximum. Chemical cementation was inferred to play a key role in domains volumetric change; a more significant role than that played by capillary in retaining the dust structure over the wetting course. The measured capillary force immediately before collapse was approximately four times less than the total destabilising inter-particle force, lending further evidence to the significance of chemical cementation in retaining the open packed domain. Cementation on Figure 6 appears in the captured hardening response of specimen. The drop in totalled inter-particle force was initially followed by constant volumetric strain (function of void ratio), lending a brittle hardening feature to the material. The greater significance of cementation forces than capillary forces lends credibility to (1) the greater risk of deflation in modern reworked soil with climate gaining more extreme patterns, (2) suitability of an array of 'surface armouring' to stabilise reworked dust accumulations including bacterial communities, e.g. cyanobacteria, in presence of sufficient sources of free calcium ions (Svirčev et al. 2013).

Fig.5

Fig.6

4. Conclusion

Deposition and deflation of airborne dust is an emerging global challenge in the light of predicted stronger aridity and winds within current climatic scenarios. Wind soil erosion and formation of dust plums have health and environmental implications, particularly at the

margins of natural dust sources (e.g. Saharan and Sahel of North Africa) as well as modern dust sources. The controls on the trigger of dust deflation into the atmosphere is yet poorly known, particularly when particulate matters (silt-sized quartz) are combined with other minerals and develop a range of size distributions and inter-particle forces. There is a need, therefore, for these controls to be identified for the purpose of planning and implementing appropriate mitigation measures. Since deflation takes place for a mean surface wind force greater than soil cementation-capillary forces combined (i.e. fluid threshold), an estimation of particle-level forces is key to any dust flux trigger modelling attempt.

This paper described a semi-empirical model for estimation of inter-particle forces in loose Aeolian fine silts with clay and carbonate inclusions. A suite of identical reworked dust specimens were simulated through wet Aeolian deposition of clay-coated silts followed by cyclic wetting-drying chemical treatment to produce Aragonite/Calcite bonds. Benchmark specimen contained 70% quartz silt (by weight) with a marked mode on 10-20μm (PM_{10}), 20% carbonate (<2μm), and 10% kaolinite (<2μm) - not untypical of much of the earth's quaternary aerosols. For a range of water contents, inter-particle forces were approximated through logging the mean particle and pore size, mean hydraulic head, matric suction, void ratio and ambient conditions. Temporal bonding forces supplied by secondary reprecipitated carbonates were observed to be four times that of capillary forces, playing the primary role in maintaining the open and loosely-cemented dust domains.

Acknowledgement

This project was partially supported by a European Grant for South-Africans grant with additional micro-analytical support for the project provided by the European Regional

Development Fund (ERDF). We also appreciate the assistance of the School of Geography facilities at the University of Leicester in Laser Diffraction Spectrometry for this study and the Newcastle University staff of the Civil Engineering and Geosciences School for providing helpful comments over an invited talk on initial findings.

References

Alfaro SC, Gaudichet A, Gomes L, Maille M. (1998) Mineral aerosol production by wind erosion : aerosol particle sizes and binding energies. Geophysical Research Letters 25:991-994.

Andrade JE, Tu X (2009) Multiscale framework for behavior prediction in granular media Mechanics of Materials 41:652-669

Arya LM, Leij FJ, Van Genuchten MT, Shouse PJ (1999) Scaling parameter to predict the soil water characteristic from particle-size distribution data Soil Science Society of America Journal 63:210-519

Arya LM, Paris JF (1981) A physicoempirical model to predict the soil moiture characteristic from particle-size distribution and bulk density data Soil Science of America Journal 45:1023-1030

Arya LM, Paris JF (1982) Reply to comments on: A physicoempirical model to predict the soil moisture characteristic from particle-size distribution and bulk density data Soil Science Society of America Journal 46:1348-1349

Assadi A (2014) Micromechanics of collapse in loess. the University of Birmingham

Assadi A, Jefferson I, O'Hara-Dhand K, Smalley I (2014) Micromechanics of quartz sand breakage in a fractal context Geomorphology 211:1-10.

Assadi A, Jefferson I (2013) Collapsibility in calcareous clayey loess: A factor of stress-hydraulic history. International Journal of GEOMATE 5(1):620-627.

Assadi A, Yasrobi SS (2012) Drainage controlled uniaxial swelling cell vol 166. Proceedings of the ICE - Geotechnical Engineering.

Assallay AM (1998) Structure and Hydrocollapse behaviour of loess. Loughborough University

ASTM (2014) D4546-14 Standard Test Methods for One-Dimensional Swell or Collapse of Soils.

Bagnold RA (1941) The physics of blown sand and desert dunes. New York: Methuen.

Bear J (1972) Dynamics of fluids in porous media. Dover, New York

BS (1990) BS 1377-5:1990 Methods of test for soils for civil engineering purposes. Compressibility, permeability and durability tests.

Claudin P, Bouchaud JP, Cates ME, Wittmer JP (1998) Models of stress fluctuations in granular media Physical Review E 57:4441-4457

Creyssels M, Dupont P, Ould el Moctar A, Valance A, Cantat I, Jenkins JT, Pasini JM, Rasmussen KR. 2009. Saltating particles in a turbulent boundary layer: experiment and theory. Journal of Fluid Mechanics. 625:47-74.

Cornelis WM, Gabriels D, and Hartmann R (2004) A parameterisation for the threshold shear velocity to initiate deflation of dry and wet sediment. Geomorphology 59:43-51.

Cundall PA, Strack ODL (1979) Discrete numerical-model for granular assemblies Geotechnique 29:47-65

Cundall PA, Strack ODL Modelling of microscopic mechanisms in granular material. In: Jenkins JT, Satake M (eds) US-Japan seminar on new models and constitutive relationships in the mechanics of granular materials, 1983.

Dantu P Contribution a l'etude mecanique et geometrique des milieux pulverulents. In: 4th International conference of soil mechanics, 1957. pp 144-148

Fredlund DG, Rahardjo H (1993) Soil mechanics for unsaturated soils. John Wiley & Sons Inc.,

Ginoux P, Prospero JM, Torres O, Chin M (2004) Long-term simulation of global dust distribution with the GOCART model: correlation with North Atlantic Oscillation. Environmental Modelling & Software 19 (2): 113–128.

Goossens D. (2004) Effect of soil crusting on the emission and transport of wind-eroded sediment: field measurement on loamy soil. Geomorphology. 58:145-160.
Graf WH (1984) Hydraulics of sediment transport. Water Resources Publications, Highlands Ranch, Colorado
Guo N, Zhao J (2013) The signature of shear-induced anisotropy in granular media Computers and Geotechnics 47:1-15
Haverkamp R, Parlange (1982) Comments on: A physicoempirical model to predict the soil moisture characteristic from particle-size distribution and bulk density data Soil Science Society of America Journal 46:1348-1349
Ishizuka M, Mikami M, Leys J, Yamada Y, Heidenreich S, Shao Y, McTainsh GH. Effects of soil moiture and dried raindroplet crust on saltation and dust emission. Journal of Geophysical Research. 113(D24212)
Lamb H (1994) Hydrodynamics. Trinity College, Cambridge University Press, Cambridge, UK
Maher BA, Prospero JM, Mackie D, Gaiero D, Hesse PP, Balkanski Y (2010) Global connections between aeolian dust, climate and ocean biogeochemistry at the present day and at the last glacial maximum. Earth-Science Reviews 99:61-97
Marticorena B, Bergametti G, Aumont B. Callot Y, N'Doume C, Legrand M (1997) Modelling the atmospheric dust cycle 2. Simulation of Saharan dus sources. Journal of Geophysical Research. 102(D4):4387-4404.
Mikami T, Kamiya H, Horio M (1998) Numerical simulation of cohesive powder behavior in a fluidized bed Chemical Engineering Science 53:1927-1940
Miller RL, Tegen I, Perlwitz J (2004) Surface radiative forcing by soil dust aerosols and the hydrologic cycle. Journal of Geophysical Research-Atmospheres 109 (D4).
Noborio K (2001) Measurement of soil water content and electrical conductivity by time domain reflectometry: a review Computers and Electronics in Agriculture 31:213-237
O'Hara-Dhand K, Assadi A, Jefferson I, Smalley I The Control of Loess Grain Shape on Size Distribution Data. In: Neild J, Wilson R (eds) 19th Windy Day: UK aeolian research community meeting, University of Southampton, 2013.
Ostojic S, Somfai E, Nienhuis B (2006) Scale invariance and universality of force networks in static granular matter Nature 439:828-830
Ravi S, Zobeck TM, Over TM, Okin GS, D'Odorico P (2006) On the effect of moisture bonding forces in air-dry soils on threshold friction velocity of wind erosion. Sedimentology 53:597–609.
Santamarina JC (2003) Soil behavior at the microscale: Particle forces. In: Germaine JT, Sheahan TC, Whitman RV (eds) Soil Behavior and Soft Ground Construction. Geotechnical Special Publication. Amer Soc Civil Engineers, New York, pp 25-56
Shao Y et al. (2011) Dust cycle: An emerging core theme in Earth system science Aeolian Research 2:181-204
Smalley IJ. (1970) Cohesion of small particles and the intrinsic resistance of simple soil systems to wind erosion. Journal of Soil Science 21:154-161.
Soulié F, Cherblanc F, El Youssoufi MS, Saix C (2006) Influence of liquid bridges on the mechanical behaviour of polydisperse granular materials International Journal for Numerical and Analytical Methods in Geomechanics 30:213-228 doi:10.1002/nag.476
Svirčev Z et al. (2013) Importance of biological loess crusts for loess formation in semi-arid environments Quaternary International 296:206-215
Thornton C, Barnes DJ (1986) Computer simulated deformation of compact granular assemblies Acta Mechanica 64:45-61
USEPA (2013) Particulate Matter (PM). United States Environmental Protection Agency

Figure Captions

Figure 1. Mode size distribution of testing aerosol identical specimens

Figure 2. Effective bearing area as a function of packing state

Figure 3. Liquid bridge geometry between pair of quartz spheres

Figure 4. Variation of inter-particle forces on the dry-to-wet stress state surface

Figure 5. Timed variation of water tension and void ratio upon wetting

Figure 6. Timed variation of cohesive inter-particle forces (balanced destabilising inter-particle forces) upon wetting

Table Captions

Table 1 Selective outputs from the DE model

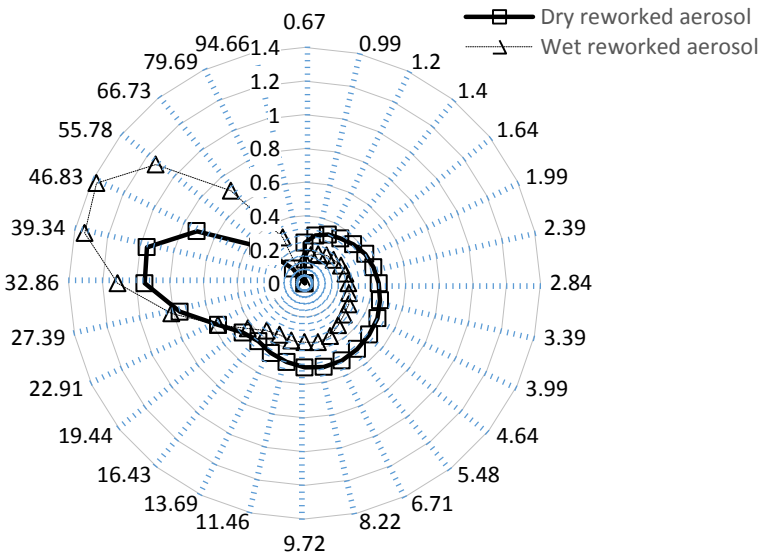
Dry reworked aerosol
Wet reworked aerosol
0.67
0.99
1.2
1.4
1.64
1.99
2.39
2.84
3.39
3.99
4.64
5.48
6.71
8.22
9.72
11.46
13.69
16.43
19.44
22.91
27.39
32.86
39.34
46.83
55.78
66.73
79.69
94.66
1.4
1.2
1
0.8
0.6
0.4
0.2
0

Fig. 1.

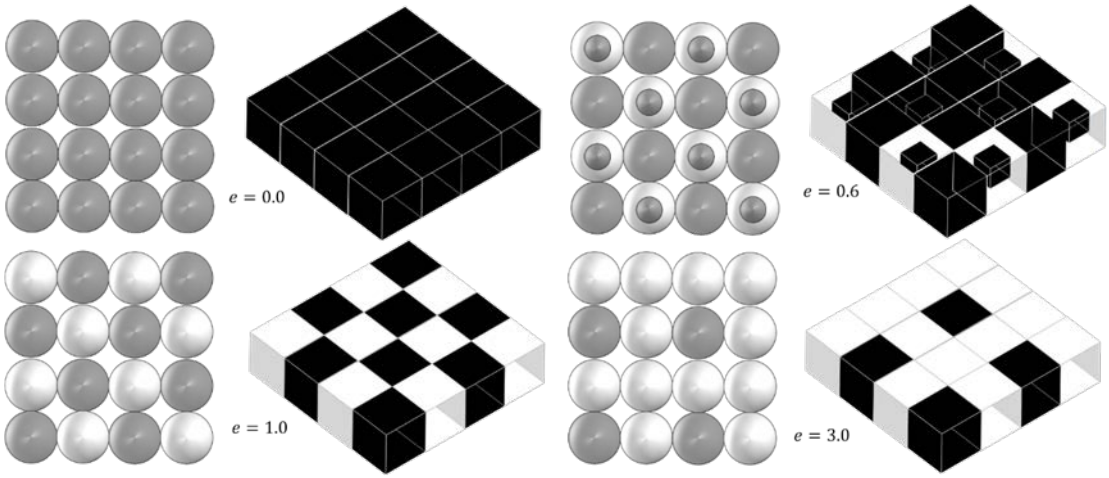
e = 0.0
e = 0.6
e = 1.0
e = 3.0

Fig. 2.

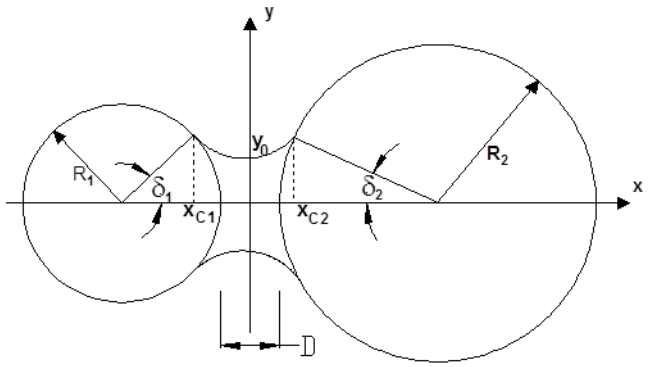
y
x
y_0
R_1
R_2
δ_1
δ_2
x_{C1}
x_{C2}
D

Fig. 3.

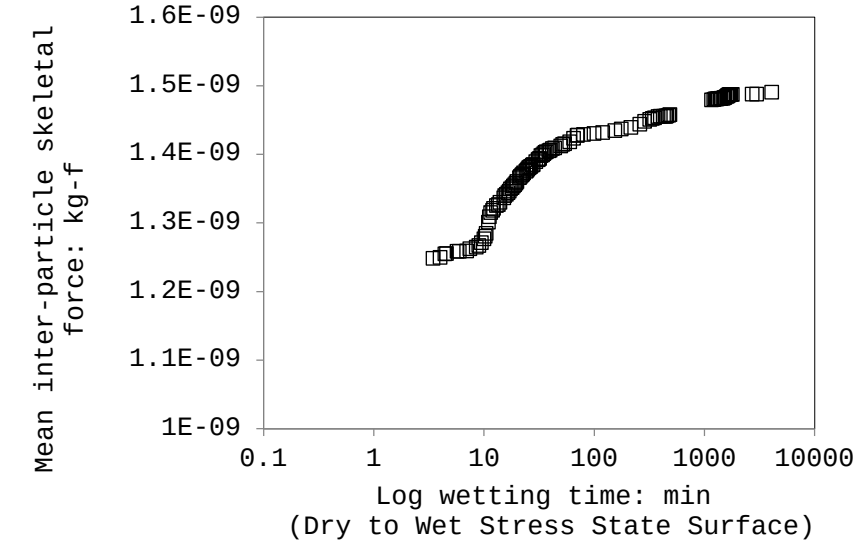
Mean inter-particle skeletal force: kg-f
1.6E-09
1.5E-09
1.4E-09
1.3E-09
1.2E-09
1.1E-09
1E-09
0.1
1
10
100
1000
10000
Log wetting time: min
(Dry to Wet Stress State Surface)

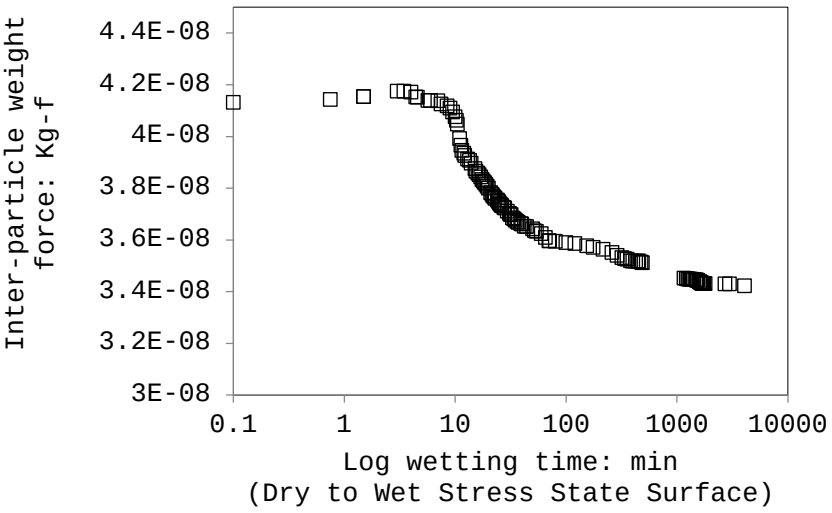
Inter-particle weight force: Kg-f
4.4E-08
4.2E-08
4E-08
3.8E-08
3.6E-08
3.4E-08
3.2E-08
3E-08
0.1
1
10
100
1000
10000
Log wetting time: min
(Dry to Wet Stress State Surface)

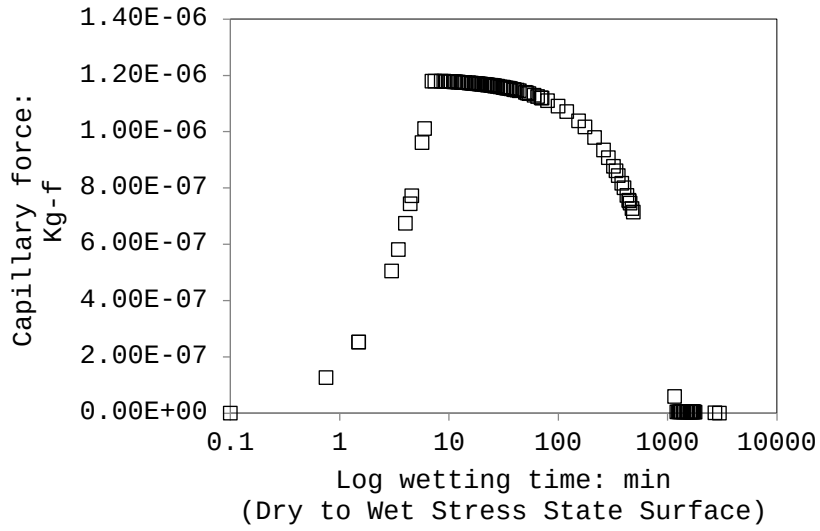
Capillary force: Kg-f
1.40E-06
1.20E-06
1.00E-06
8.00E-07
6.00E-07
4.00E-07
2.00E-07
0.00E+00
0.1
1
10
100
1000
10000
Log wetting time: min
(Dry to Wet Stress State Surface)

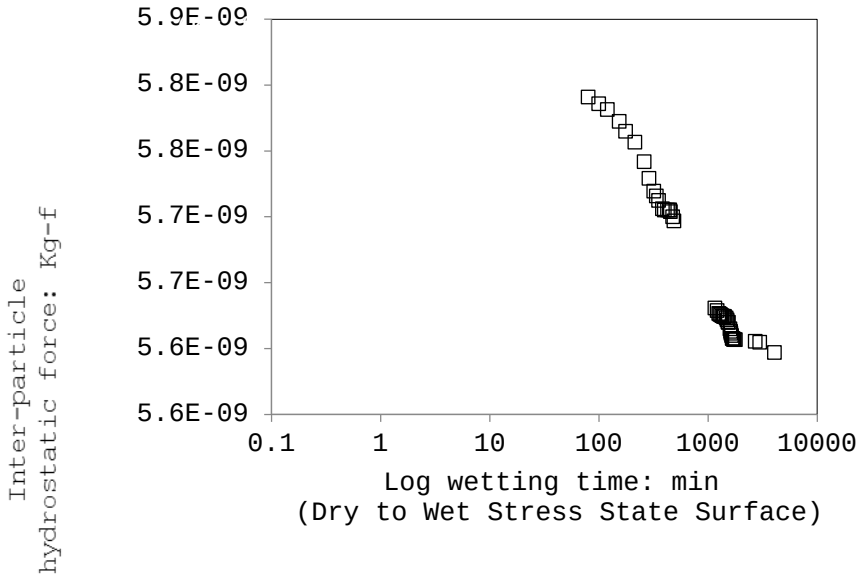
Inter-particle hydrostatic force: Kg-f
5.9E-09
5.8E-09
5.8E-09
5.7E-09
5.7E-09
5.6E-09
5.6E-09
0.1
1
10
100
1000
10000
Log wetting time: min
(Dry to Wet Stress State Surface)

Fig. 4.

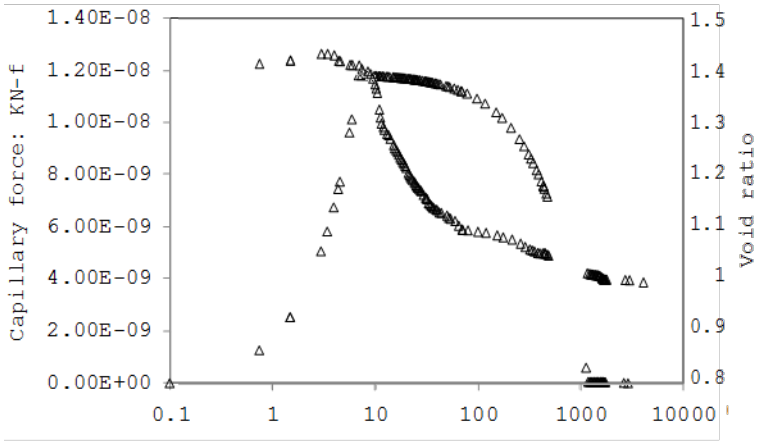
Capillary force: KN-f
Void ratio
1.40E-08
1.20E-08
1.00E-08
8.00E-09
6.00E-09
4.00E-09
2.00E-09
0.00E+00
1.5
1.4
1.3
1.2
1.1
1
0.9
0.8
0.1
1
10
100
1000
10000

Fig. 5.

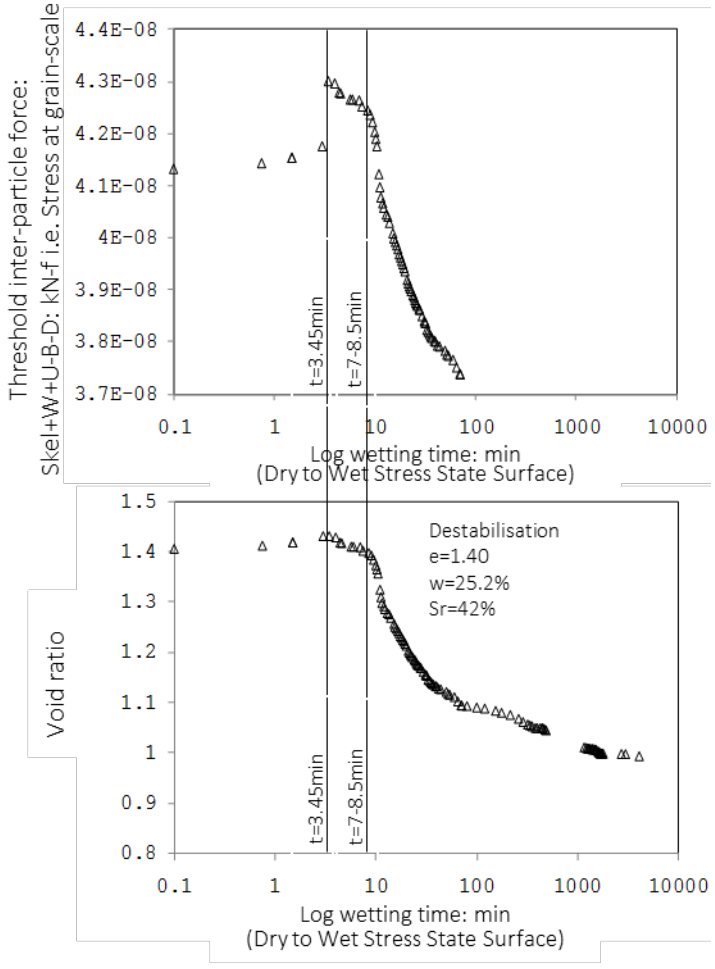
Threshold inter-particle force:
Skel+W+U-B-D: kN-f i.e. Stress at grain-scale
4.4E-08
4.3E-08
4.2E-08
4.1E-08
4E-08
3.9E-08
3.8E-08
3.7E-08
t=3.45min
t=7-8.5min
0.1
1
10
100
1000
10000
Log wetting time: min
(Dry to Wet Stress State Surface)
Void ratio
1.5
1.4
1.3
1.2
1.1
1
0.9
0.8
Destabilisation
e=1.40
w=25.2%
Sr=42%
t=3.45min
t=7-8.5min
0.1
1
10
100
1000
10000
Log wetting time: min
(Dry to Wet Stress State Surface)

Fig. 6.

Tables

Table 1 Selective outputs from the DE model

Void ratio	Effective area (cubic expression) – A_e	Effective area (spherical expression) – A_e	Mean normal contact force
0.000	4 d^2	$(\pi/2)$ 4d^2	$(\pi/2)\sigma'$ 4d^2
0.286	2.67 d^2	$(\pi/2)$ 2.67 d^2	$(\pi/2)\sigma'$ 2.67 d^2
0.330	3 d^2	$(\pi/2)$ 3 d^2	$(\pi/2)\sigma'$ 3 d^2
0.385	2.44 d^2	$(\pi/2)$ 2.44 d^2	$(\pi/2)\sigma'$ 2.44 d^2
0.600	2.5 d^2	$(\pi/2)$ 2.5 d^2	$(\pi/2)\sigma'$ 2.5 d^2
0.800	2.22 d^2	$(\pi/2)$ 2.22 d^2	$(\pi/2)\sigma'$ 2.22 d^2
1.000	2 d^2	$(\pi/2)$ 2 d^2	$(\pi/2)\sigma'$ 2 d^2
1.250	1.67 d^2	$(\pi/2)$ 1.67 d^2	$(\pi/2)\sigma'$ 1.67 d^2
1.286	1.625 d^2	$(\pi/2)$ 1.625 d^2	$(\pi/2)\sigma'$ 1.625 d^2
1.670	1.5 d^2	$(\pi/2)$ 1.5 d^2	$(\pi/2)\sigma'$ 1.5 d^2
2.200	1.25 d^2	$(\pi/2)$ 1.25 d^2	$(\pi/2)\sigma'$ 1.25 d^2
2.600	1.11 d^2	$(\pi/2)$ 1.11 d^2	$(\pi/2)\sigma'$ 1.11 d^2
3.000	1 d^2	$(\pi/2)$ 1 d^2	$(\pi/2)\sigma'$ 1 d^2
>3.000	1 d^2	$(\pi/2)$ 1 d^2	$(\pi/2)\sigma'$ 1 d^2

Appendix 1 [Supporting document]. An example of Arya-Paris function output

$W_s = 74.1\ g$

$e = 1.05, \gamma_w = 0.001\ g/mm^3, G_s = 2.65$

$\gamma_s = 2.65 \times 1 = 2.65\ g/cm^3$

D_i: μm		$\overline{R_i}$: cm	W_i		Passing %	n_i	Y	α_i	$n_i^{1-\alpha_i}$	r_i: cm
0.5	1.0	3.75E-05	0.0765	0.0765	7.65	1.3062E+11 *	15.67431 **	1.4100 ***	2.7650E-05	1.6488E-07 ■
1.0	2.0	0.000075	0.1123	0.1888	18.88	2.3991E+10	14.95218	1.4405	2.6784E-05	3.24569E-07
2.0	3.0	0.000125	0.0814	0.2702	27.02	3755859806	13.93841	1.4557	4.3281E-05	6.87653E-07
3.0	4.0	0.000175	0.0615	0.3317	33.17	1033259315	13.08376	1.4514	8.5201E-05	1.35073E-06
4.0	5.0	0.000225	0.0562	0.3879	38.79	444655155	12.45914	1.4407	0.00015448	2.33846E-06
5.0	6.0	0.000275	0.0434	0.4314	43.14	188135734	11.7707	1.4225	0.00031898	4.10702E-06
6.0	7.0	0.000325	0.0377	0.4690	46.90	98854309	11.2244	1.4039	0.00058958	6.59881E-06
7.0	8.0	0.000375	0.0307	0.4997	49.97	52424842	10.6628	1.3813	0.00113957	1.05855E-05
8.0	9.0	0.000425	0.0300	0.5297	52.97	35243650	10.3008	1.3649	0.00176303	1.4922E-05
9.0	10	0.000475	0.0260	0.5558	55.58	21896948	9.8579	1.3429	0.00303679	2.18881E-05
10	20	0.00075	0.1788	0.7345	73.45	38178091	10.3743	1.3683	0.00161252	2.51838E-05
20	30	0.00125	0.1025	0.8371	83.71	4730481	8.3857	1.2563	0.01946169	0.000145817
30	40	0.00175	0.0661	0.9032	90.32	1110438	6.9735	1.1535	0.1180204	0.000502717
40	50	0.00225	0.0433	0.9456	94.56	342384	5.8533	1.0576	0.47994500	0.001303424
50	60	0.00275	0.0303	0.9768	97.68	131309	4.9795	0.9728	1.37635407	0.002697771
60	70	0.00325	0.0131	0.9899	98.99	34303	3.8395	0.8465	4.96366216	0.006054688
70	77	0.00367	0.0101	1.0	100.00	18368	3.3486	0.7853	8.23024414	0.008815989
			Sum=1							

* $n_i = \dfrac{3 \times 0.0765}{4\pi.(3.75 \times 10^{-5})^3.2.65} = 1.3062 \times 10^{11}$

** $Y = \dfrac{Y_F.Y_i}{Y_i + (Y_f - Y_i)exp[-\mu(x+\Delta x)]} - \Delta Y = \dfrac{19.686 \times 0.719}{0.719 + (19.686 - 0.719).e^{\{-0.457 \times (0.684 + Log\ (1.3062 \times 10^{11}))\}}} - 1.902 = 15.67431$

*** $\alpha_i = \dfrac{Log\ N_i}{Log\ n_i} = \dfrac{Y}{Log\ n_i}$

■ $r_i = 3.75 \times 10^{-5} \sqrt{\dfrac{4 \times 1.0488 \times 2.765 \times 10^{-5}}{6}} = 1.6488 \times 10^{-7}\ cm$